JOURNAL OF MATERIALS SCIENCE 20 (1985) 303–315

A study of ultrafine porosity in hydrated cements using small angle neutron scattering

D. PEARSON*, A. J. ALLEN‡
Materials Development Division and ‡Materials Physics Division, AERE Harwell, Didcot, Oxfordshire, UK

Small angle neutron scattering makes use of the neutron contrast due to differences in the scattering power between small, particulate regions and the general background medium, and has only very recently been applied to study the porosity in hydrated cement systems. The technique is applied to pore sizes below approximately 30 nm and produces data on pore size distribution, pore volume and pore shape without recourse to drying techniques and the potential structural degradation which may occur. Results indicate a bi-modal pore size distribution at approximately 5 and 10 nm diameter, with a total volume accounting for some several percent of the total cement block. The best estimate of the 5 nm pore shape is considered to be curved-faced tetrahedra. The pores appear to be relatively unaffected by changes in the water-to-cement ratio or accelerating admixture investigated, but macro defect free cement does show significant pore structure alteration.

1. Introduction

Small angle neutron scattering (SANS) has been used as a technique to characterize matrix inhomogeneities in a variety of materials [1] ranging from precipitates in metals [2], to pores in clays [3]. The SANS technique is most powerful as it produces data from a macroscopic and representative section of the cement, requires no specimen drying pretreatment, and generates data on pore size distribution, total pore volume and pore shape. The inhomogeneities considered are small even by electron microscopy standards, typically 1–100 nm in diameter. Recent work at Harwell [4, 5] has applied SANS methods to the study of hardened cement pastes (HCP), working in the range 3–30 nm. The initial work clearly showed that the inhomogeneities in cement, giving rise to scattering at diameters less than 30 nm, are pores.

The preliminary results [4, 5] led to several conclusions:

1. HCP contains a bimodal distribution of fine pores with diameters of approximately 5 and 10 nm.

2. There is about 2% of porosity with diameters below 10 nm.

3. The pores under investigation are probably of low eccentricity or even spherical.

4. Water-to-cement ratio seems to have a negligible effect on the size distribution of the pores below 30 nm, and only a small effect on the porosity.

5. Specimen pretreatment can significantly alter structures at sizes below 30 nm.

The work reported here is a continuation of the initial study. Some of the experiments have been repeated in order to investigate reproducibility of data and continued for longer counting times both to improve statistics and to obtain improved Porod plots. Additional samples have been studied both to generate more basic data thus permitting the refinement of the analysis, and to study specific cement systems which might be expected to show different ultrafine pore size distributions.

2. Preparation of specimens

2.1. General preparation

Six samples were studied over a two day period using the SANS spectrometer on the PLUTO reactor at Harwell. Four of the six were from an identical batch ($A1$–$A4$) but with different treat-

0022–2461/85 $03.00 + .12

ments. In sample $B1$, the hydration was accelerated with calcium chloride. The final sample $C1$, was a "macro defect free" (MDF) cement supplied by Oxford University.

The A and B type samples were made from standard, OPC, brought in from the kiln site and used within one month of purchase. They were mixed in a rotary, low-shear mixer for five minutes, distilled water (for samples $A1$–$A4$) or a $CaCl_2$ solution made with distilled water (for sample $B1$) was added and then mixing continued for a further five minutes. Six specimens of type A and six of type B were made in 32 mm diameter right cylinder moulds, approximately 50 mm high, and were hand tamped. In each case, one of the six was used for the SANS experiment and the remainder for other tests (see Section 3).

All A and B type samples were stored for five days in a saturated, high humidity environment at ambient temperature and then stored underwater at 20°C for times dependent on the treatment schedule and sequence of scattering experiments. All specimen cutting was done on a water flooded diamond wheel to produce small coupons approximately 10 mm x 10 mm x 0.9 mm thick, in order to fit into standard SANS sample cells. This thickness gives sufficient small angle scattering without any danger of multiple scattering. The samples were sealed in standard quartz optical cells during SANS measurements in order to prevent moisture being pumped out by the spectrometer's vacuum system.

2.2. SANS samples $A1$–$A4$

All had a 0.6 water-to-cement (w/c) ratio. After 20 days immersion in water, the SANS samples were cut from one specimen of the six manufactured and then placed back in water. The individual storage conditions were as follows:

$A1$: Stored a total of 25 days underwater.

$A2$: Stored a total of 23 days underwater. Partially dried over LiCl for 24 h and then stored in heavy water (D_2O) until tested (approximately 36 h).

$A3$: Stored a total of 24 days underwater. Oven dried for 24 h at 105°C and then rewetted by storing in water until tested (approximately 40 h).

$A4$: Stored a total of 23 days underwater. Partially dried over LiCl for 24 h and then stored in deuterated methanol (CD_3OD) until tested (approximately 30 h).

2.3. SANS sample $B1$

This sample was made with a solution of 2 wt% Analar calcium chloride in distilled water at a 0.2 liquid/cement ratio and stored under water for 25 days.

2.4. SANS sample $C1$

The sample was produced by Oxford University using a standard OPC with a small addition of polymer and a very low w/c ratio and then processed by twin roll milling in a manner which results in a so-called MDF [6] cement. Curing followed their preferred route and the specimen then remained dry for approximately 24 days prior to irradiation. Cutting was performed on a dry diamond wheel, finally producing samples for the standard SANS cells of similar dimensions to A and B types.

3. Determination of physical parameters

3.1. Strength

After using one of the six 32 mm right cylinder specimens to prepare the SANS A or B samples, the remaining five specimens in each case were available for compressive strength measurements in order to assess their uniformity.

Three weeks after manufacture, the specimens were machined on a water-flooded diamond wheel to give parallel ends. They were then either tested in the surface wet state or stored, again underwater, for later testing (some of the fracture pieces were stored underwater for later displacement pycnometric measurements).

The compressive test machine was a Contest 250 kN type which conforms to British Standard BS 1881 and ASTM requirements. The data on the cylinders were converted to a BS "4 inch cube stress" using conversion constants previously obtained [7].

This test was used solely to indicate uniformity of mix and comparability between sample types A, B and C. The statistical nature of strength measurements in cement systems leads to relatively large variations between individual samples and these results (shown in Table 1) should, therefore, only be considered as being comparative.

Type C specimens were cut from a flat disc of material on a dry diamond wheel. Six specimens were cut, one of which was further sliced to allow

TABLE I Compressive strength of samples

Specimen type	Compressive strength (MPa) (mean)			
	21 days		32 days	
A	61.5 57.6 62.8	(60.6)	56.0 52.0	(54.0)
B	47.0 54.6 38.6	(46.7)	47.2 48.8	(48.0)

insertion into the SANS holder. The mechanical test performed on the remaining five specimens was a flexural test using centre point loading. This test was performed dry and approximately 3 weeks after manufacture. Pieces from the flexural test were then stored dry for use in displacement pycnometric measurements.

3.2. Pycnometry

Water displacement pycnometry (the details of which appear elsewhere [8]) was performed on fracture pieces of the specimens on approximately the same day as the samples were studied by SANS (about 30 days after they were made). Pycnometry gives values for the total porosity and density of the samples. Values given in Table 2 are in fact the mean of measurements performed on three separate specimens.

4. SANS applied to cement systems

4.1. The small angle neutron scattering technique

The technique makes use of the neutron contrast due to differences in the scattering power between small, particulate regions or pores in a sample and the general background medium. The contrast between these particulate regions and the surrounding material causes a small component of the incident beam to be scattered through a small angle with respect to the straight on direction. The width, intensity and profile of the scattered component yields information on the mean size, volume fraction, size distribution and shape of the scattering particles or pores. The SANS of interest, with the instrumental configuration used, occurs at less than five degrees.

The SANS spectrometer at Harwell is described both in reference [9] and in our original papers [4, 5]. The scattering data, which are collected on the instrument's 2-dimensional, position-sensitive detector, are radially averaged about the centre of the scattering pattern (the straight through beam direction). The resulting scattering intensity $I(Q)$ is thus given as a function of Q (the magnitude of the change in neutron wave vector $\mathbf{Q} = 4\pi/\lambda \sin(\phi/2)$ with λ the neutron wavelength and ϕ the angle of scatter).

A normalized "empty cell" run is abstracted to remove the background scattering. A "water-filled cell" is also run and normalized, and the actual sample scattering is divided by this. Thus the sample scattering at a given $\mathbf{Q}$ is given as a multiple of the water scattering at the same $\mathbf{Q}$. Another run is performed using cadmium (which is a neutron absorber) and is used to correct for electronic noise in the detector and associated electronics.

4.2. Theory of the method of analysis [10]

In neutron scattering, it is convenient to describe an interaction between a neutron beam and the sample by the macroscopic cross-section for the process. The attenuation of the incident beam due solely to some process, j, in a sample of thickness τ is $e^{-\Sigma_j \tau}$, where Σ_j is the macroscopic cross-section for the process. For thin samples $\Sigma_j \tau$ is the fraction of the incident beam undergoing the process in the sample. In SANS, the fraction of the incident beam scattered into a solid angle element $d\Omega$ in a direction specified by the angle of scatter is $\tau(d\Sigma/d\Omega)$ where $(d\Sigma/d\Omega)$ is the macroscopic, differential, small angle scattering from the sample. This fraction is most simply found by comparing the small angle scattering from the sample with the random, isotropic, incoherent scattering from water which, unlike the specimen, contains no particulate regions. As water is an incoherent, isotropic scatterer with a well known cross-section

TABLE II Density and porosity of samples using pycnometry and the subsequently calculated degree of hydration

Specimen type	Mean density ($g\,cm^{-3}$)	Mean porosity (%)	Deduced degree of hydration (%)
A	1.51	40.0	65
B	1.43	44.4	61
C	2.39	13.8	36

Σ_w, the normalized scattered intensity for water at any Q should be given for small $\Sigma_w \tau_w$ by:

$$I(Q)_w = \frac{\Sigma_w \tau_w}{4\pi} \quad (1a)$$

where τ_w is the thickness of the water sample in the cell. However, the 1 mm standard water thickness is such that $\Sigma_w \tau_w$ is not small, and work by Sears [11] shows that the self extinction of the water incoherent scattering must be taken into account. A very good approximation for the correct sample SANS cross-section, results if the expression for $I(Q)_w$ is divided by the water transmission constant T_w, to give an effective $I(Q)_{w\,eff}$:

$$I(Q)_{w\,eff} = \frac{\Sigma_w \tau_w}{4\pi} \times \frac{1}{T_w} \quad (1b)$$

Provided that the small angle scattering does not attenuate the beam too greatly, the small angle scattering cross-section for the sample is given by multiplying the ratio of sample-to-water scattering at any particular point by the factor in Equation 1b.

The full equation, taking account of background, noise, volumes of sample and water (V_s and V_w), incoherent scattering in the sample (FB) and attenuation of the beam (sample and water transmission constants T_s and T_w), is:

$$\frac{d\Sigma}{d\Omega}(Q) = \left[\frac{\left(\frac{S_i}{M_s} - \frac{C_i}{M_{Cd}}\right) - T_s\left(\frac{C_i}{M_c} - \frac{Cd_i}{M_{Cd}}\right)}{\left(\frac{W_i}{M_w} - \frac{Cd_i}{M_{Cd}}\right) - T_w\left(\frac{C_i}{M_c} - \frac{Cd_i}{M_{Cd}}\right)} - FB \right] \times \frac{T_w V_w}{T_s V_s} \times \frac{I(Q)_{w\,eff}}{\tau_w} \quad (2)$$

A more complete derivation and explanation of the terms can be found in Ghosh [12]. (Because of the extinction effect in water, T_w in Equation 2 cancels with T_w in the expression for $I(Q)_{w\,eff}$ in Equation 1b. Sears' results indicate that this is a good approximation because the correction to allow for actual absorption of neutrons in water, cancels with the forward scattering enhancement associated with the slab sample geometry.)

4.3. Approximations

Having obtained the basic differential scattering cross-section ($d\Sigma/d\Omega$) as a function of the change in neutron wave vector ($\mathbf{Q}$), the small angle scattering (generally at less than five degrees) can be divided into two distinct regions:

i. At low scattering angles when $QR_G \lesssim 2.5$, the Guinier approximation holds [10] and

$$\frac{d\Sigma}{d\Omega}(Q) = N_{PT} V_{PT}^2 \times (\text{contrast}) \times \exp\left(\frac{-Q^2 R_G^2}{3}\right)$$

or more simply

$$\frac{d\Sigma}{d\Omega}(Q) = (\text{volume fraction}) \times V_{PT} \times (\text{contrast}) \times \exp\left(\frac{-Q^2 R_G^2}{3}\right) \quad (3a)$$

where Q is the magnitude of change in neutron wave vector, N_{PT} is the number density of scattering particles, V_{PT} is the volume of a scattering particle with radius of gyration R_G, and R_G is the radius of gyration of the scattering particle. The contrast term is given in Section (4.5) below.

This expression assumes that all the particles are of the same shape and are randomly orientated. Thus, a plot of $\ln(d\Sigma/d\Omega)$ vs Q^2 (known as the Guinier plot) has a gradient of $-R_G^2/3$.

ii. At larger scattering angles ($QR_G \gtrsim 3$), the Porod approximation holds [10] and

$$\lim_{Q\to\infty} \frac{d\Sigma}{d\Omega}(Q) = N_{PT} \times (\text{contrast}) \times 2\pi \times S_{PT} \times \frac{1}{Q^4}$$

or

$$\lim_{Q\to\infty} \frac{d\Sigma}{d\Omega}(Q) = (\text{volume fraction}) \times 2\pi \left(\frac{S_{PT}}{V_{PT}}\right) \times (\text{contrast}) \times \frac{1}{Q^4} \quad (4a)$$

where S_{PT} is the surface area of a particle which has a radius of gyration R_G.

iii. The Porod region can be combined with the overall scattering data to produce a third approximation equation [10]

$$\frac{\lim_{Q\to\infty}\left(Q^4 \frac{d\Sigma}{d\Omega}\right)}{\int_0^\infty \left(Q^2 \frac{d\Sigma}{d\Omega}\right) dQ} = \frac{1}{\pi}\left(\frac{S_{PT}}{V_{PT}}\right) \quad (5a)$$

This equation differentiates between specific shapes of scattering particle.

iv. Equations 3a, 4a and 5a apply directly to

one specific particle size within a generalized background medium. In our case, however, a pore size distribution occurs and so a range of particles with different R_G exists and the appropriate sum or average over the porosity size distribution must be taken.

After integrating over the porosity size distribution, the Guinier approximation can still be applied to that part of the distribution for which $QR_G \lesssim 2.5$. If this region forms a separate population of pores, well separated in size from those for which the Guinier region does not apply, then a linear region appears on the Guinier plot (provided the Porod law scattering from larger pores is small). The Guinier region can be extrapolated back to zero Q for absolute cross-section measurements (see Fig. 4a) and the Guinier equation for this component alone becomes:

$$\frac{d\Sigma}{d\Omega}(\mathbf{Q}) = \begin{pmatrix}\text{volume fraction of}\\ \text{Guinier population}\end{pmatrix} \times \overline{V_{PT}} \times (\text{contrast}) \times \exp\left(\frac{-Q^2R_G^2}{3}\right) \quad (3b)$$

where $\overline{V_{PT}}$ is the mean volume and R_G^2 is the ratio of the means $\overline{R_G^5}/\overline{R_G^3}$. These means are taken over the porosity size distribution defined in terms of the distribution of R_G. Thus for any quantity $X(R_G)$

$$\bar{X} = \frac{\int_0^\infty V(R_G)\,N(R_G)\,X(R_G)\,dR_G}{\int_0^\infty V(R_G)\,N(R_G)\,dR_G}$$

where $N(R_G)$ is the number size distribution function and $V(R_G)$ is the volume of a pore of radius of gyration R_G. This method of definition is in fact precisely equivalent to that obtained by the porosity size distribution analysis of mercury intrusion porosimetry (i.e. the plot of dV/dr against r).

The Porod approximation holds for all pores in the size distribution given by $QR_G \gtrsim 3$, and for the case where there are no finer pores, Equation 4a becomes:

$$\lim_{Q\to\infty} \frac{d\Sigma}{d\Omega}(Q) = \text{contrast} \times 2\pi \times S_{\text{Total}} \times \frac{1}{Q^4} \quad (4b)$$

where S_{Total} is now the total surface area of pores per unit volume of sample. The biggest contribution to this total surface area is that from the very large number per unit volume of the very finest pores, but there are also smaller contributions from larger pores. Thus, for a given pore shape, direct comparisons of the Guinier and Porod parts of the scattering curve can be used to give an upper limit to the surface-to-volume ratio (strictly S/V^2) of the fine pores.

In averaging Equation 5a over the porosity size distribution, the equation is modified to:

$$\frac{\lim_{Q\to\infty}\left(Q^4\frac{d\Sigma}{d\Omega}\right)}{\int_0^\infty\left(Q^2\frac{d\Sigma}{d\Omega}\right)dQ} = \frac{1}{\pi}\left(\overline{\frac{S_{PT}}{V_{PT}}}\right) \quad (5b)$$

where $(\overline{S_{PT}/V_{PT}})$ is the mean surface to volume ratio of the complete porosity size distribution, provided that $d\Sigma/d\Omega$ in the denominator is taken as the actual scattering curve over the whole Q range. Again the major contribution to $(\overline{S_{PT}/V_{PT}})$ is that from the smallest pores, but larger pores will contribute, tending to reduce the overall mean. Thus, assuming a given pore shape, the surface to volume ratio obtained from Equation 5b can be taken as a lower limit for the fine pores. Alternatively, if $d\Sigma/d\Omega$ is determined by extrapolating the linear Guinier region back to zero Q (see Fig. 4a), a value of surface to volume ratio in agreement with that obtained from Equations 3b and 4b should result.

4.4. The pore size distribution

Certain particle shapes such as spheres, long cylinders or discs, each produce specific analytical functions for $d\Sigma/d\Omega(\mathbf{Q})$. For each of these shapes, a computer program by Vonk [13] varies the particle size distribution whilst checking for correlation with the normalized experimental data until an optimum particle size distribution is obtained. By comparing the goodness of fit for the different specified shapes used in the Vonk program, information about the shape may be deduced.

Our original papers [4, 5] discussed these considerations and the conclusion drawn was that the scattering particles were in fact close to spherical. The Vonk program has again been used in order to derive the particle size distribution for each of the specified shapes in turn, and thence predicted values have been obtained for mean volume and surface-to-volume ratios in each case. These may then be compared to the values derived from the Guinier and Porod region data (see Fig. 1).

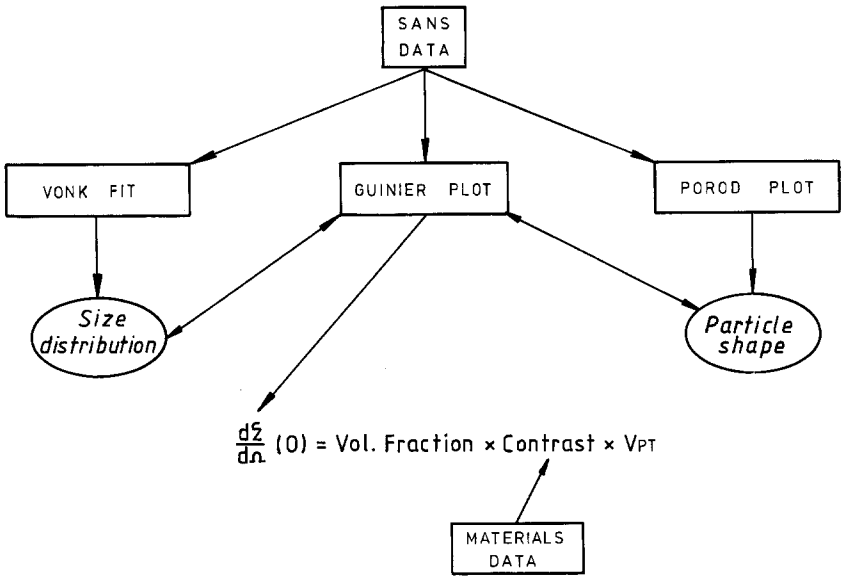

Figure 1 Simplified block diagram showing inter-relation of data and data analysis.

4.5. SANS contrast within HCP

The basic method of determining the neutron scattering contrast was fully discussed in the earlier papers. The method entails approximating the volume of phases present in the HCP and then producing the coherent scattering length density P_b*. The scattering length density of the matrix $P_{b\ \text{average medium}}$ is considered to be $\Sigma^{\text{all phases}}$ $(P_{b\ \text{phase}}\ V_{\text{phase}})$ where V_{phase} is the fraction of the phase.

The SANS contrast is then obtained as $(P_{b\ \text{particle}} - P_{b\ \text{average medium}})^2$. The identity of the particle giving rise to the scattering need not be initially known; particle phases may be assumed, their SANS contrast calculated and then checked with the original scattering for correlation between different sample runs.

4.6. Volume concentration of scatterers

The Guinier approximation can be used to derive the volume fraction of scatterers. From Equation 3b, we can see that at zero change in the neutron wave vector, the equation simplifies to:

$$\frac{d\Sigma}{d\Omega}(0) = (\text{volume fraction}) \times (\text{contrast}) \times \overline{V_{PT}} \tag{6}$$

The term $d\Sigma/d\Omega(0)$ can be found from the Guinier plot of ln $(d\Sigma/d\Omega)$ vs Q^2, by extrapolating the linear region back to zero Q. The contrast is obtained having decided the scattering particle and background composition. The effective volume $\overline{V_{PT}}$ may be deduced from the Vonk distribution having first decided the shape of the scattering particles from Equation 5b. (This volume can be checked by independently deriving the volume from R_G in the Guinier plot.)

5. Experimental data

5.1. Strength

Table I gives the compressive strength of specimen types A and B at 21 days after manufacture and 32 days after manufacture. The values are consistent with normal statistical variations in cement. By way of comparison, the MDF cement (specimen C) had a mean flexural strength of approximately 65 MPa (probably of the order of ten times stronger than the other specimens).

5.2. Pycnometry

Table II gives porosity and density results from the water displacement pycnometric measurements. Quite clearly, the MDF specimen has a much higher density and much lower porosity than the samples manufactured by the more normal processing route.

*P_b is the product of the mean neutron scattering length per atom in the phase and the atomic number density of the phase.

5.3. Small angle neutron scattering

Fig. 1 shows schematically how the Vonk fit, Guinier and Porod plots, can be cross-related and used to obtain the maximum information on the particles or pores causing small angle scattering.

5.3.1. Vonk distributions

The Vonk program considers three particle shapes – discs, long cylinders, and spheres. Although the previous paper concluded that spheres gave the most accurate fit, the three shapes were again tried with these new data. As before, the fit for long cylinders or spheres was considerably better than that for discs, and the fit for spheres was slightly better than that for cylinders.

Equations 4b and 5b indicate surface-to-volume ratios consistent with globular particles rather than long cyclindrical particles. For simplicity, spherical particles have therefore been assumed initially for the derivation of other results (but see also the discussion).

The Vonk distribution for the specimens are shown in Figs. 2 and 3. They all tend to show a peak at around 5 nm diameter with the exception of C1 (the MDF specimen). The lowest size-peak for MDF seems to be at a significantly smaller size of about 2.5 nm diameter.

Another peak is generally apparent at around 10 nm diameter, except in the case of the MDF specimen which has the distribution shifted to smaller sizes (about 7 nm). The plots are all normalized to give the largest peak (5 nm)) equal to one unit and little information can be inferred from the relatively small variation in heights of the other peaks. Rather surprisingly, the dried and rewetted sample has a very similar distribution to the $0.6\,w/c$ water stored specimen. This is a significant result when one considers the result from the previous series of experiments [4], when the dried specimen showed a significantly different structure which now seems to have been almost totally regenerated.

A further peak is apparent at about 27 nm diameter for all specimens. This peak is approaching instrumental limits, but has been preliminary confirmed recently using a SANS spectrometer covering a different particle size range.

5.3.2. Guinier and Porod plots

Examples of both the Guinier and Porod plots (for samples A1) are shown in Fig. 4. The Guinier plot of $\ln(d\Sigma/d\Omega)$ vs Q^2 clearly shows a linear region corresponding to the strong peak in the Vonk distribution function at 5 nm diameter. The Porod plot of $\ln(d\Sigma/d\Omega)$ vs $\ln Q$ also shows a Porod region over a range of Q appropriate for particles of diameter 5 nm and greater.

The Porod tail exhibits a Q^{-4} dependence which is itself indicative of a true three-dimensional shape. Shapes with one or two dimensions either very large or very small compared to $1/Q$ (such that fewer than three dimensions contribute to the measured small angle scattering), would give Porod tails with a different Q dependence [10, 13] e.g. Q^{-1} for thin needles, Q^{-2} for thin discs or wide slabs, Q^{-3} for long cylinders. At lower Q values, the Porod plot displays a linear region of gradient -2.7 which appears to be associated with the 10 nm pore population seen in the Vonk size distribution. This is consistent with a porosity size distribution which tails off with size as $1/R_G^{1.3}$. It is hoped to report on SANS work concentrating in this size range in the near future.

An increased count time of 12 h was used for samples A1 and A2, enabling Porod data to be obtained which is well above background noise. These data can then be used to obtain surface-to-volume ratios with greater accuracy than was possible in the previous experiments which used count times of approximately 6 h.

Table III shows data derived using both Equation 3b and 4b (upper limit), and Equation 5b (lower limit), and also shows theoretical (S/V) for spheres and tetrahedra. The table gives values obtained from data in the previous series of experiments as well as those in this series.

5.3.3. Contrast

The calculation of the background scattering length density has been carried out in a similar manner to the procedure used in the previous paper. The pycnometry was used to obtain an indicative degree of hydration and this is given with the pycnometric data in Table 2. Using this "characteristic" degree of hydration, approximating the stoichiometric equations for hydration, and taking estimates of initial phase make-up, phase densities, and coherent neutron scattering lengths, the overall background scattering length density was obtained.

Consistent with previously obtained data, it has been assumed that the scattering particles are pores. Calculations have been performed considering that the pores can be air-filled or water-filled or, in some cases, filled with D_2O (A2), or CD_3OD (A4).

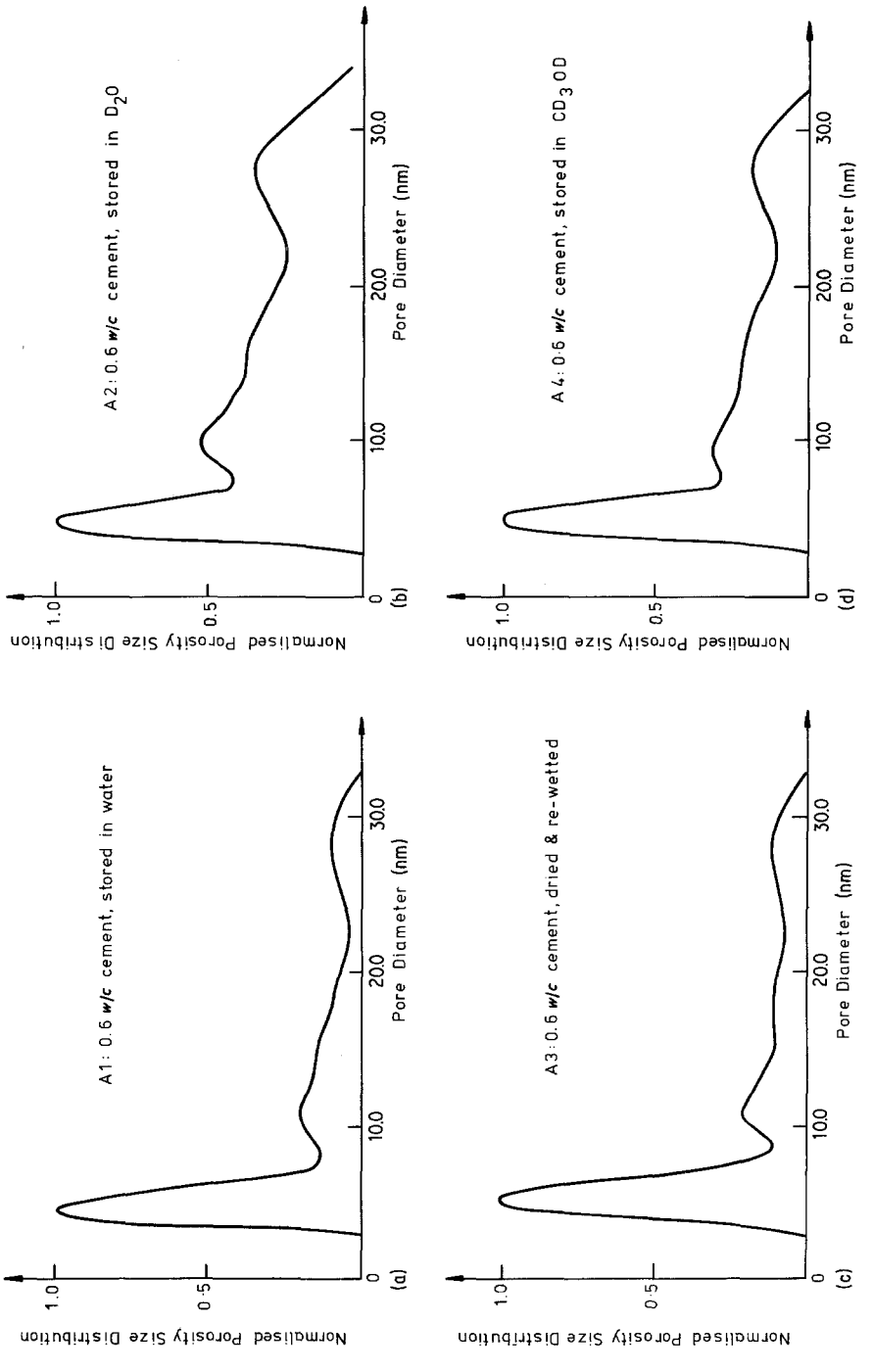

Figure 2 Vonk distributions for A-type specimens (assuming spheres).

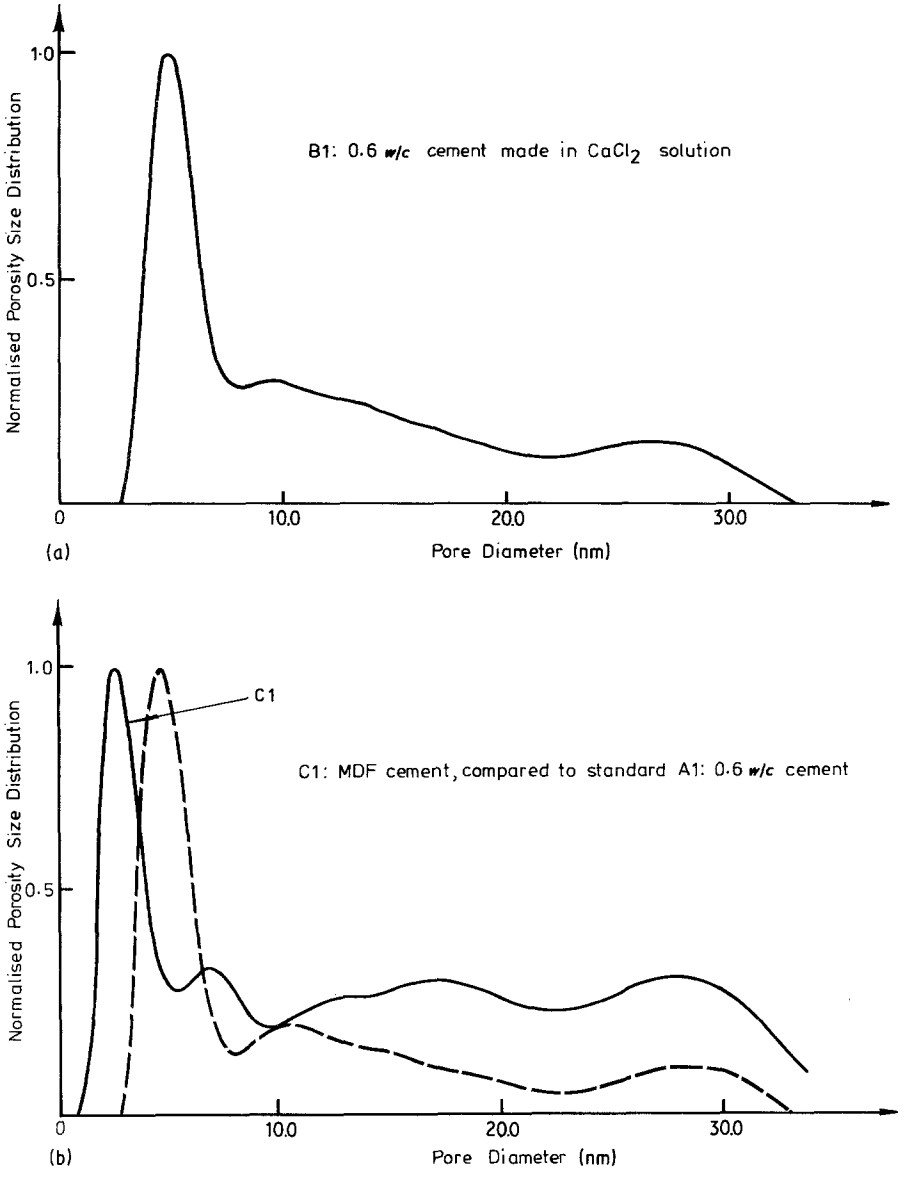

Figure 3 Vonk distributions for specimens B and C (assuming Spheres).

5.3.4. Pore volume

In our original papers, [4, 5], values were quoted for possible volume concentrations of pores and gel particles on the assumption that these were spherical. We have now refined our method of analysis by including a better correction for extinction effects in the scattering data, a correction which increases the porosities previously quoted. As described later, departures from spherical shape also increase the porosities.

Fig. 4a also shows how the Guinier plot is extrapolated back to zero Q, such that, having obtained the contrast and V_{PT}, the volume concentration of pores can be calculated. The value of $\bar{V}_{PT}$ necessarily assumes spheres. If different shapes were to be considered then the relationship between volume and radius of gyration would change (for a Gaussian porosity distribution of spheres centred on a diameter D_0 and of standard deviation σ, $\bar{V}_{PT} = \pi D_0^3/6[1 + 3\sigma^2/D_0^2]$). In general, for different shapes, $\bar{V}_{PT}$ will decrease for a given R_G, and so the volume concentration of pores will increase.

Because the 5 nm peak is so pronounced and

TABLE III Measured and theoretical surface-to-volume ratios of specimens

Specimen*	Guinier radius R_G (nm)	Measured (S/V) ratio (nm^{-1})		Theoretical (S/V) ratio (nm^{-1})	
		Porod Equation 4	Porod and integrated scattering Equation 5	Sphere	Tetrahedron (flat face)
A	2.36	2.9	1.4	0.98	1.7
B	2.10	3.4	1.9	1.1	1.9
C	2.56	2.6	1.6	0.91	1.6
D	2.51	3.9	1.5	0.93	1.6
A1	2.10	2.4	2.0	1.1	1.9
A2	2.26	1.9	1.0	1.0	1.8
A3	2.28	–	1.8	1.0	1.8
A4	2.26	–	1.4	1.0	1.8
B1	2.19	–	1.5	1.1	1.8
C1	1.32	3.0	–	1.8	3.0

*A–D refer to data from Pearson *et al.* [4] and Allen *et al.* [5]. A1–A4, B1 and Cl refer to this work.

is reasonably well separated from larger pore sizes, it is safe to carry out a simple Guinier extrapolation from this peak alone.

If we now assume that the gel has the "characteristic" degree of hydration calculated, we get the porosities shown in Table IV (for spheres). Also included in Table IV are the results from the previous series of experiments, recalculated in an identical manner to these recent results.

6. Discussion

6.1. Size distribution

The results obtained in this second series of experiments are in broad agreement with the first series. A peak at approximately 5 nm is confirmed in all cases except the MDF sample which seems to have its complete distribution shifted to smaller sizes. Again, a 10 nm peak is seen in all except the MDF sample and there is some evidence (although by no means conclusive) of another larger peak in the distribution at around 27 nm.

6.2. Drying and rewetting

The dried and rewetted sample (*A*3) seems to have completely regenerated its fine pore structure. This may be construed as indicating a structure which collapses on drying but which can be re-expanded on rewetting.

6.3. Accelerated hydration

The addition of $CaCl_2$ (*B*1) (which is a well known cement accelerator) seems to have little effect on the pore structure (and so, we assume on the gel particles). This sample should be compared with the 0.2 *w/c* specimen in the first series of experiments (sample *A*). Although $CaCl_2$ accelerates

TABLE IV Volume fraction of porosity in specimens (assuming spheres)

Specimen	Peak diameter (nm)	Guinier radius R_G (nm)	Volume weighted mean volume $\bar{V}_{PT}$ (m^3) ($\times 10^{-26}$)	$d\Sigma/d\Omega$ at $Q = 0$ (m^{-1} sterad)$^{-1}$	Porosity (%)		
					H_2O filled in hydrated cement	Air filled in hydrated cement	D_2O filled in deuterated cement
A	4.65	2.36	5.26	15.2	1.01	1.45	N.A.
B	4.60	2.10	5.10	22.1	1.74	2.51	N.A.
C	5.55	2.56	8.95	8.9	0.19	0.24	1.74
D	4.50	2.51	4.77	10.8	9.18	13.04	N.A.
A1	4.50	2.10	5.73	17.9	1.39	2.03	N.A.
A2	4.85	2.26	7.17	40.8	1.12	1.39	11.14
A3	5.00	2.28	7.66	33.3	1.92	2.77	N.A.
A4	4.85	2.26	7.17	76.7	4.69	6.93	6.93*
B1	4.85	2.19	6.93	26.0	1.81	2.61	N.A.
C1	2.45	1.32	1.10	0.7	N.A.	0.53	N.A.

*CD_3OD filled pores in deuterated cement.

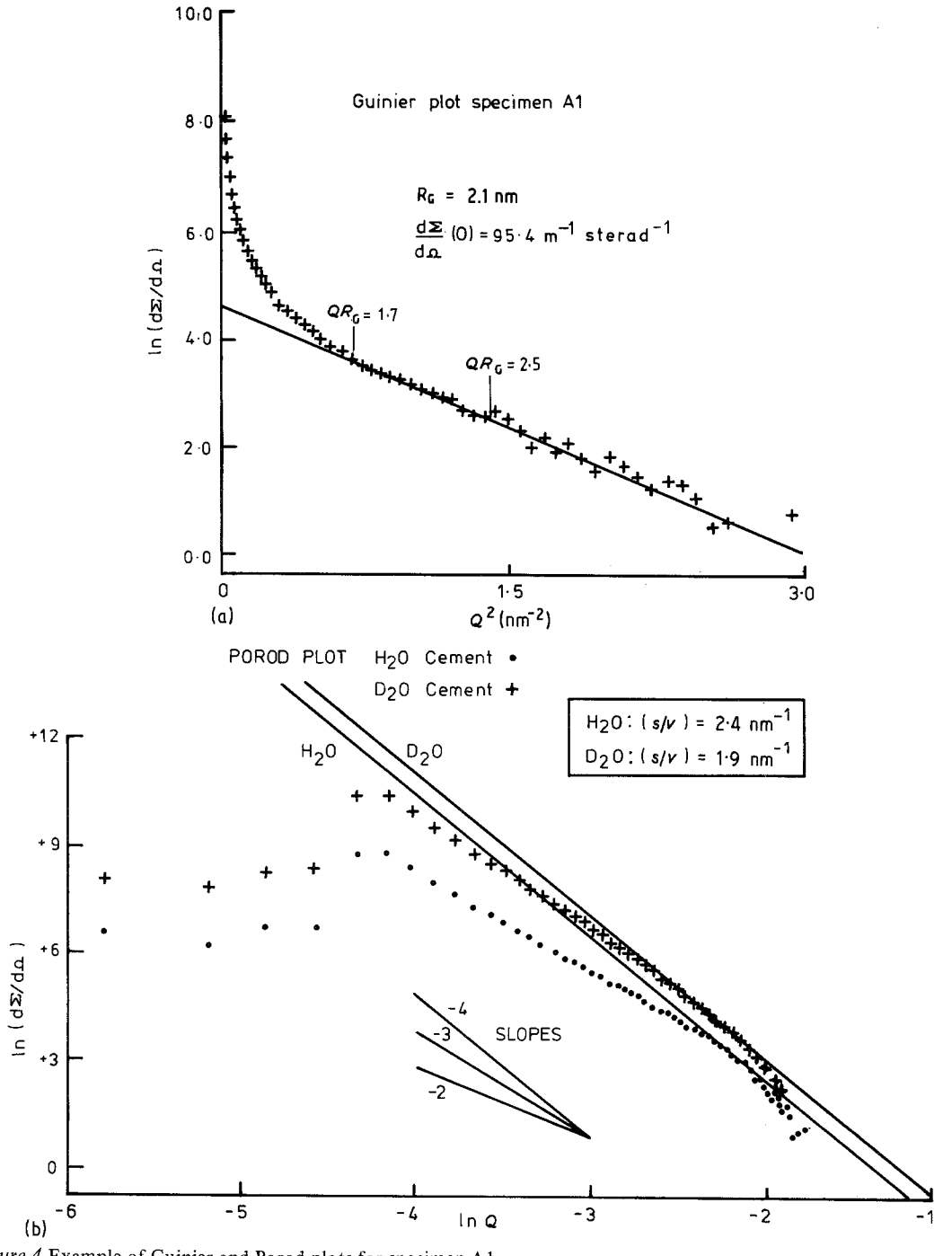

Figure 4 Example of Guinier and Porod plots for specimen A1.

hydration, there seems to be no gross effect on either the size distribution or the volume concentration of pores after this storage sequence; experiments are in hand, however, to look at gel porosity in accelerated pastes at early times.

6.4. MDF cement

The most significant structural alteration seems to occur with the MDF cement (*C*1). The small addition of polymer has not been considered when calculating the phase make-up or degree of hydration of the cement, but we would not expect these factors to in any way explain the much smaller size distribution observed. The very low *w/c* ratio used in preparing this sample leads us to believe that hydration continues until all

available water has been used up and the sample thus contains air-filled pores. The marked strength increases which are apparent with MDF cements, have been attributed to the removal of the large flaws which act as Griffith-type crack initiation sites [6]. This work would imply that the polymer addition or the mechanical working, or a combination of the two, has modified the ultrafine pore sizes and thus, we assume, the gel particles. Work by Alford *et al.* [14] using ion beam thinned specimens has shown however that the appearance of MDF get in TEM micrographs is not significantly different from normally prepared OPC, although the calcium hydroxide does seem to appear as smaller particles with some degree of disorder.

6.5. Pore shape

Of the three shapes which can be tested by the Vonk plot, spheres again produce the best fit. Although spheres have been assumed in deriving the other parameters, the theoretical (S/V) for spheres is always lower than that produced by calculations based on the scattering data using Equations 4 or 5. The tentative model which we have assumed considers that the calcium-silicate-hydrate gel particles themselves are spherical and that the scattering which we are seeing is due to pores at the interstices of well packed gel spheres. Although a sphere, where $(S/V) = 3/R_G(3/5)^{1/2}$, is a fairly good approximation to these spaces, a more correct approximation would be tetrahedra, where $(S/V) = 18/R_G(20)^{1/2}$. The value of S/V for tetrahedra is also given in Table 3, these values have increased over those for spheres and now fall very closely indeed to the values calculated from equations 4 and 5. If the faces of the tetrahedra were now assumed to be curved (a much more exact approximation to the shape of interstices in a model structure of close packed spheres) then the theoretical (S/V) could quite easily increase to the marked (S/V) obtained from the Porod equation.

As before, the volume concentration of fine pores (if assumed to be spheres) is found to be low. The results for the D_2O exchange specimen ($A2$), however, appears to have risen considerably as compared with the first experiment, this we believe to be the result of a failed quartz cell, allowing the sample to be evacuated during the 12 h run. The much stronger scattering observed for CD_3OD specimens ($A4$) cannot, however, be explained purely by changes in contrast between pores and gel, a genuinely greater fine pore porosity seems to be indicated. This could be connected with the fact that methanol has a much lower surface tension than that of the water (7.3×10^{-2} Nm^{-1} for H_2O against 2.3×10^{-2} for CH_3OH).

6.6. The effect of shape on porosities

It was mentioned earlier that if different shapes to spheres were assumed, $\bar{V}_{PT}$ would generally decrease resulting in an increase in the volume concentration of pores. For the same R_G, $V_{TET}/V_{SPHERE} = 0.64$, thus the volume of fine pore porosity must be increased by a factor of 1.56 to go from spheres to flat-faced tetrahedra. For concave-faced tetrahedra, $V_{CONC\ TET}/V_{SPHERE}$ could lead to a multiplication factor of two or three times the values in Table 4. Note that for a given shape, all the porosity volume concentrations would be increased by the same factor; the relative porosities are not disturbed.

Table 4 assumes that the gel has developed to the "characteristic" degree of hydration and compositions are assumed as discussed in the previous paper. If we assume greater hydration, then in the case of water-filled pores the contrast will be slightly reduced and hence the porosity increased. This effect, however, is small compared to the effect of shape. Work is at present in hand to obtain more accurate data on the degree of hydration of cement specimens used in SANS experiments.

In general then, the cements can be assumed to have a well defined concentration of ultrafine pores – possibly sufficient in volume to account for a significant proportion of the discrepancy found between pycnometric measurements and mercury intrusion porosimetry [15]. The MDF cement has a lower concentration of fine pores, these also being at a different size range to those found for the other specimens.

7. Conclusions

7.1. Confirmation of previous results

The following conclusions, derived from the preliminary experiments [4, 5], have been confirmed:

1. There is a bimodal distribution of pores in HCP at diameters of approximately 5 and 10 nm.

2. Assuming spheres, there is about 2% of porosity with diameters below 10 nm.

3. The pores are spherical or near spherical rather than being long and filamentary.

7.2. New results

In addition, the following new results have been obtained:

1. Calcium chloride has little effect on the porosity or pore size distribution of HCP in the range investigated.

2. Rewetting a previously dried specimen appears to regenerate the fine pore structure.

3. Concave-faced tetrahedra appear to be a more accurate approximation to the actual pore shape.

4. For 0.6 *w/c* specimens which have not been dried, estimates of the volume concentration of 5 nm pores vary between a minimum of approximately 1.5%, assuming spherical shape, to a maximum of 6% for concave tetrahedra.

5. The peak at 10 nm appears to mark the lower limit of a size distribution of pores which tails off as $1/R_G^{1,3}$.

6. The ultrafine porosity in macro defect-free cement appears to be significantly different from conventional HCP.

Acknowledgements

The authors would like to thank D. D. Double, R. A. J. Sambell, P. Schofield and C. G. Windsor for their useful comments during the preparation of this text.

References

1. H. WALTHER and P. PIZZI, "Small Angle Neutron Scattering for Non-destructive Testing" Chap. 10, p. 341. Research Techs for NDT 4, edited by R. S. Sharp (Academic Press, London, 1980).
2. P. CARTESE, P. PIZZI, H. WALTHER, G. BERNADINI and A. OLIVI, *Mater. Sci. and Eng.* **36** (1978) 81.
3. D. J. CEBULA, R. K. THOMAS, N. M. HARRIS, J. TABONY and J. W. WHITE, *Discussions of the Faraday Society* **65** (1978) 76.
4. D. PEARSON, A. J. ALLEN, C. G. WINDSOR, N. McN. ALFORD and D. D. DOUBLE, *J. Mater. Sci.* **18** (1983) 430.
5. A. J. ALLEN, C. G. WINDSOR, V. RAINEY, D. PEARSON, D. D. DOUBLE and N. McN. ALFORD, *J. Phys. D.* **15** (1982) 1817.
6. J. D. BIRCHALL, A. J. HOWARD and K. KENDALL, *Nature* **289** (1981) 388.
7. R. A. J. SAMBELL, AERE Harwell, unpublished data.
8. N. McN. ALFORD, *Cem. and Conc. Res.* **10** (1980) 263.
9. D. PAGE, AERE Report R9878 (1978).
10. A. GUINIER and G. FOURNET, "Small angle scattering of X-rays" (J. Wiley and Sons, New York, 1955).
11. V. F. SEARS, *Adv. Phys.* **24** (1975) 1.
12. R. E. GHOSH, "A computing guide for small angle scattering experiments", p. 166. ILL Report 81GH29T (1981).
13. C. G. VONK, *J. Appl. Cryst.* **9** (1976) 433.
14. N. McN. ALFORD, G. W. GROVES and D. D. DOUBLE, *Cem. Conc. Res.* **12** (1982) 349.
15. D. N. WINSLOW and S. DIAMOND, *J. Mater.* **5** (1970) 564.

Received 1 March
and accepted 13 March 1984